

# RESONANCE STRUCTURES IN THE IMPEDANCE OF A CERAMIC BREAK AND THE MEASURED RESULTS

Y. Shobuda, T. Toyama, J-PARC Center, JAEA/KEK, Ibaraki, Japan  
Y.H. Chin, K. Takata, KEK, Ibaraki, Japan

## Abstract

Recently, we have developed a new theory to evaluate longitudinal and transverse impedances of any size of ceramic break sandwiched between metal chambers. The theory successfully reproduces the resonance structures in the impedance due to trapped modes inside the ceramic break. The comparisons between the theoretical and the simulation results such as ABCI and CST Studio show excellent agreements, indicating that they can be used as a good benchmark test for accuracy of simulation codes. To demonstrate the existence of such resonances, the transverse impedance of the ceramic break is measured using the wire-method. The measurement results reproduce the simulations well. The theory is particularly useful for the evaluation of the impedance of the ceramic break with titanium nitride coating.

## INTRODUCTION

A short ceramic ring sandwiched by metal chambers is called a ceramic break. Such ceramic breaks are often inserted between the chambers near bending magnets in proton synchrotrons. Their purpose is to mitigate the eddy current effects over the chambers excited by the outside time-varying magnetic fields, and the induced magnetic turbulence is confined in the chamber between the ceramic breaks [1].

On the other hand, capacitors are typically attached on the outer surface of the ceramic breaks as RF shields to prevent the radiation fields to propagate out of the ceramic breaks. The radiated fields may cause malfunctioning of devices along the accelerators.

In the J-PARC main ring (MR), two ceramic breaks have been additionally installed since 2011. At first, they forgot to attach RF shields around them. When the beam with particles more than  $3.75 \times 10^{13}$  was shot into MR, they discovered that the power source of the quadrupole magnets were suddenly tripped, and the noise level in the adjacent monitors were increased intolerably high. The problems were put under control by attaching RF shields around the ceramic breaks. This accident reminded them the importance of the RF shields to the ceramic breaks.

In the rapid cycling synchrotron (RCS) in J-PARC, titanium nitride (TiN) is coated on the inner surface of the ceramic chambers, to suppress the secondary emission of electrons, caused by the collisions between a part of a proton beam and the chamber surface. The TiN coating is supposed to prevent the build-up of the electron cloud from destabilizing the beams [2, 3].

These ceramic breaks become also sources of the beam impedance [4, 5]. The precise estimation of impedance is an important step toward realization of high intensity beams

in proton synchrotrons [6]. Recently, a new theory is developed to understand the characteristic of the ceramic break impedance [7], which enables us to get an insight about the resonance structure caused by the trapped mode inside the ceramic.

Next, let us show an example of the resonance in the ceramic break.

## IMPEDANCES OF CERAMIC BREAK AND THEIR RESONANCE STRUCTURES

Let us assume that the ceramic has the dielectric constant  $\epsilon'$ . The inner and the outer radii and the length of the ceramic are  $a$ ,  $a_2$  and  $g$ , respectively. Applying the formulae (7) and (18) in the reference [7], we obtain the theoretical impedance. The longitudinal and the transverse impedances are shown in Figs. 1 and 2, respectively. For the longitudinal impedance, the real and the imaginary parts of the impedance are shown in the left and the right figures, respectively. For the transverse impedance, the real and imaginary parts of impedances are shown in the same figure by the solid and the dot lines, respectively.

The large resonance at low frequency in the transverse impedance is approximately given by

$$f \sim \frac{c}{2\pi a} \sqrt{\frac{a^2 + 1.5(a_2^2 - a^2)}{a^2 + 1.5\epsilon'(a_2^2 - a^2)}}, \quad (1)$$

which essentially shows the resonance around the circumference ( $2\pi a$ ) of the ceramic break [8]. The frequency is lowered compared to that for the vacuum gap ( $\epsilon' = 1$ ) case due to the wavelength contraction effects of the ceramic.

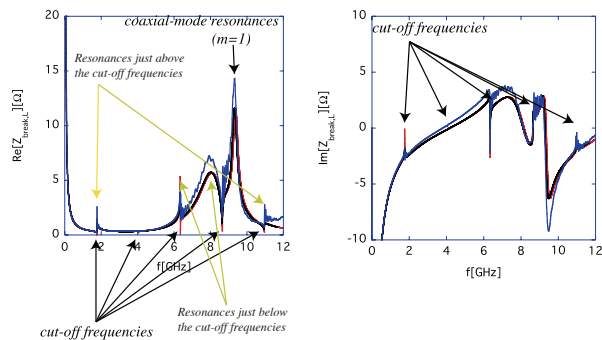


Figure 1: Longitudinal impedances of the ceramic break ( $a = 65$  mm,  $a_2 = 70$  mm,  $g = 10$  mm and  $\epsilon' = 11$ ) calculated by the theory (red), the simulation codes ABCI (black) and CST Studio (blue).

All the calculation results (the theory, ABCI [9] and CST [10]) reproduce the same resonance structures and show

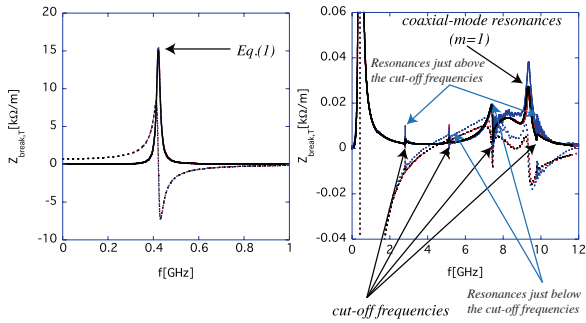


Figure 2: Transverse impedances of the ceramic break ( $a = 65$  mm,  $a_2 = 70$  mm,  $g = 10$  mm and  $\epsilon' = 11$ ) calculated by the theory (red), the simulation codes ABCI (black) and CST Studio (blue). The left and the right figures show the results up to 1 GHz frequency, and those up to 12 GHz, respectively.

good agreements between them, in particular, between the theory and ABCI. The comparison between theory and different simulation codes can indeed provide a good benchmark for accuracy test of the codes.

Next, let us discuss the resonance structure appeared in the impedance of the ceramic breaks.

### Cavity-mode Resonance

One type of resonances is characterized by the cut-off frequencies. In other words, they behave like cavity-mode resonances. The cut-off frequencies are given by

$$f_{c,L} = \frac{j_{0,k}c}{2\pi a}, \quad (2)$$

$$f_{c,T} = \frac{j_{1,k}c}{2\pi a}, \quad (3)$$

for the longitudinal and the transverse impedances, respectively, where  $j_{n,k}$  are the  $k$ -th zeros of the Bessel function  $J_n(z)$  [11]. This type of resonances appear in the impedances of the vacuum gap, as well [8].

As shown in Figs. 1 and 2, two types exist in the resonances around the cut-off frequencies. In one case, the resonance appears just above the cut-off frequency. In the other case, the resonance appears just below the cut-off frequency [12].

The physical reason for the first case (resonances just above the cut-off frequencies) is as follows. The difference of the dielectric constants between the ceramic and the vacuum introduces the reflection of waves at the boundaries. This reflection of electromagnetic fields at the lower and the upper boundaries of the ceramic creates trapped mode inside. These trapped modes can leak out of the ceramic either to the outside or the inside of the chamber. Below the cut-off frequencies, they couple with unpropagating modes inside the chamber, and the interaction between the beam and these unpropagating modes takes place only in a limited space around the ceramic location. Above the cut-off frequencies, however, the trapped modes couple with propagating modes inside the chamber and the interaction between the beam and

the propagating modes is extended for much longer distance, and as a result, the impedance is enhanced.

The second case (resonances just below the cut-off frequencies) is excited by another mechanism. The impedance of the ceramic break is approximately obtained by adding the impedances (the impedance of the gap and that of the capacitor made by the ceramic) in parallel. For a thick gap, the admittance of the ceramic break is capacitive at low and high frequency. However, there is a frequency region between them where the admittance is switched to inductive. On the other hand, the gap itself works as a capacitor below the cut-off frequencies, since the electromagnetic fields can be stored inside without propagating away through the beam chamber. As a result, the coupling between the inductance of the ceramic and the capacitance of the gap creates resonances below the cut-off frequencies in the intermediate frequency region.

### Coaxial-mode Resonance

There is another type of resonances in the ceramic break. This behaves like the coaxial-like mode whose fields are mainly localized inside the ceramic. The resonant frequencies are roughly estimated by the conditions given by

$$\frac{\partial(Y'_0(\tilde{\mu}_m a)J_0(\tilde{\mu}_m a_2) - J'_0(\tilde{\mu}_m a)Y_0(\tilde{\mu}_m a_2))}{\partial f} = 0, \quad (4)$$

$$\frac{\partial(Y'_1(\tilde{\mu}_m a)J_1(\tilde{\mu}_m a_2) - J'_1(\tilde{\mu}_m a)Y_1(\tilde{\mu}_m a_2))}{\partial f} = 0, \quad (5)$$

for the longitudinal and the transverse impedances, respectively, where

$$\tilde{\mu}_m = \sqrt{\frac{4\pi^2\epsilon'f^2}{c^2} - \frac{m^2\pi^2}{g^2}}, \quad (6)$$

$Y_n(z)$  is the Neumann function [11], and the prime in the Neumann and the Bessel functions denotes the differential with their argument  $z$ . The positive integer  $m$  is longitudinal (coaxial)-mode number, and describes the number of half-wavelengths in the ceramic. The  $m = 1$  order coaxial mode resonance is identified in Figs.1 and 2 in the shown frequency scope. The resonant frequencies are estimated as about 9.28 GHz both for the longitudinal and the transverse impedances.

At the coaxial-mode resonant frequency, the electric fields are almost parallel to the longitudinal direction at  $\rho = a$  and  $\rho = a_2$ . In other words, the fields behave like antenna both on the inner and outer surface of the ceramic, and the fields can propagate away both inside and outside of the chamber. Consequently, the impedance has sharp peaks at the frequencies.

## MEASUREMENT RESULTS

Let us experimentally study the existence of such resonance structures, especially in the transverse impedance of the ceramic break. A straightforward way to measure the transverse impedance is to use stretching twin wires inside

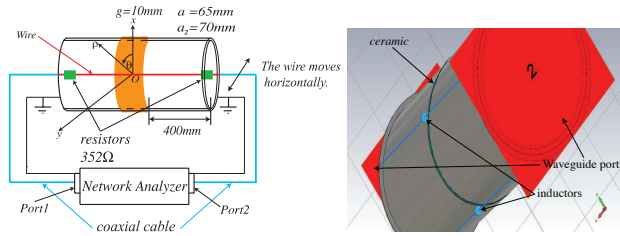


Figure 3: A schematic picture of the measurement setup. The orange in the left figure is the ceramic, which is replaced by the aluminum ring when  $S_{21}^{ref}$  is measured.

the chambers and to observe the transmission coefficients for the differential mode. However, this method has an accuracy problem, since it is critical to enhance the ratio of the signal to the noise for precise measurements.

In this regard, we decided to take another method as a first step. We measure the longitudinal impedance by using a single wire, then, evaluate the transverse impedance by changing the wire position from  $-30$  mm to  $+30$  mm by  $5$  mm step in the horizontal direction. The transverse impedance is provided by detecting the second order coefficient for the wire position in the longitudinal impedance and by dividing it by the wavelength  $k$  [13].

A schematic picture of the setup is shown in the left figure of Fig. 3. The longitudinal impedance is measured by stretching the wire with the radius  $80$   $\mu\text{m}$ . The impedance is calculated by using the standard log-formula [5]:

$$Z_L(x_w) = -2Z_{cc} \log \frac{S_{21}^{ceramic}}{S_{21}^{ref}}, \quad (7)$$

where  $Z_{cc}$  ( $\approx 402 \Omega$  in our case) is the characteristic impedance for the coaxial-structure,  $S_{21}^{ceramic}$  and  $S_{21}^{ref}$  are the transmission coefficients for the case of the ceramic break sandwiched by the aluminum chambers and for the case that the ceramic break is replaced by the reference (aluminum) ring, respectively. The transmission coefficient  $S_{21}$  is measured with 4-port Agilent technologies ENA Series Network Analyzer E5071C [14] by connecting the ports of the analyzer to the ends of the aluminum chamber through two coaxial cables. In order to assure the matching condition between the characteristic impedance  $Z_{cc}$  and the impedance of the cable  $50 \Omega$ ,  $352 \Omega$  resistors are connected at both the ends of the wire. The calibration is done by 2-port electric calibration module 85092,b.

A significant concern related to the measurement of the impedance of the ceramic break is intrinsic to that using Network Analyzer. The ceramic break has no electric path over the ceramic for DC current. The image current may find a different path from the one inside the ceramic gap for lower frequency, if the path provides a smaller impedance. It may be the internal of the Network Analyzer.

In order to cope with the effect, let us consider the model in the right figure of Fig. 3. To simulate the impedance concerning the image currents, four artificial inductors are

symmetrically connected between two waveguide ports, describing the signals from the Network Analyzer. In reality, when one terminal at the chamber is connected to one port at the Network Analyzer with  $1$  m long coaxial cable and the other terminal is done to the other port in the same way, the inductance due to the circuit composed of two cables and the Network Analyzer may be roughly estimated as a few  $\mu\text{H}$ .

Now, let us investigate the inductance dependence of the longitudinal impedance by the simulation with CST Studio [10]. The left figure of Fig. 4 shows the result for  $x_w = 0$  with  $0.9 \mu\text{H}$  inductors (red) and that with  $2 \mu\text{H}$  inductors (black). The right figure of Fig. 4 shows the simulation result of the transverse impedance evaluated by the position dependence of the longitudinal impedance with the inductances (For reference, the result without the inductors is shown by the blue lines). Those results indicate that the longitudinal impedance can be reliably measured for the frequency higher than  $0.3$  GHz, which means that the resonance peak can be clearly identified in the transverse impedance. In other words, the amount of the peak value does not depend on the inductances under consideration.

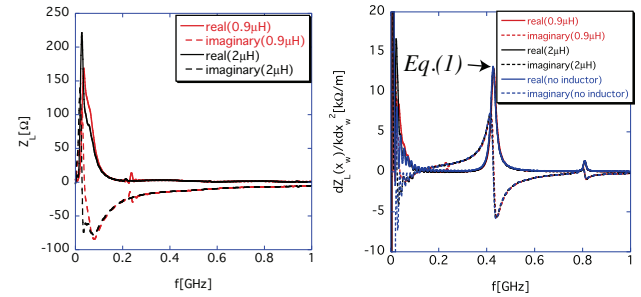


Figure 4: The inductance dependence of the simulated longitudinal impedance (left) and the corresponding result for the transverse impedance (right) evaluated by the longitudinal impedances with the several wire positions.

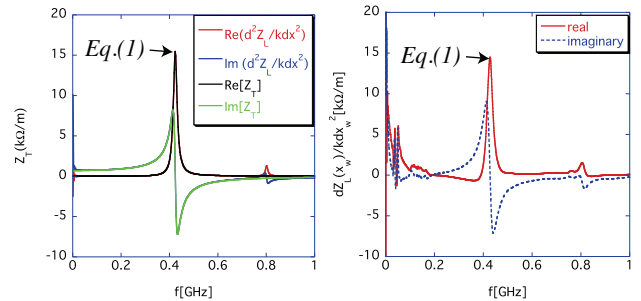


Figure 5: The simulation results by using a charged particle (left) and the wire-measurement results of the transverse impedance (right).

The right figure of Fig. 5 shows the measurement result. As expected, the measurement results at lower frequency are not reliable. Nevertheless, the resonance peak predicted by Eq.(1) can be identified. Moreover, the resonance peak around  $0.8$  GHz can be seen in the result. Such small peak

is visible also in the simulation result shown in the right figure of Fig. 4. But, notice that the peak does not appear in the original transverse impedance shown in the left figure of Fig. 2. In the simulation results, the transverse impedance is calculated according to its definition. Namely, it was done by integrating the transverse wake field excited by the horizontally shifted source particle (not the wire) along the center of the chamber, and by dividing it by the amount of the value of the horizontal position of the particle.

However, the longitudinal impedance measured by the shifted wire is equivalent to the impedance evaluated by integrating the longitudinal electric field along the same path as that on the shifted source particle, because the position of the witness particle and that of the source particle cannot be distinguished in this measurement setup. In order to demonstrate the speculation, let us calculate the longitudinal impedances by using a charged particle with and without the horizontal shift, where the integration path of the longitudinal electric field is identical to the path of the source particles. After that, let us evaluate the transverse impedance by detecting the position dependence of the longitudinal impedances. The red and blue lines in the left figure of Fig. 5 show the real and the imaginary parts of the results, respectively. For reference, the real and the imaginary parts of the transverse impedance based on the definition are shown by the black and green lines, respectively. While the resonance given by Eq. (1) is identical for both the cases, the small resonance peak around 0.8 GHz is missing in the black and green lines. From this excise, we can conclude that the peak around 0.8 GHz in the right figure of Fig. 5 is artificially created by intrinsic errors associated with the evaluation scheme of the transverse impedance by using the longitudinal impedance.

The measured result (the right figure of Fig. 5) is reliable, because it well-reproduces both the simulation results in the right figure of Fig4 and in the left figure of Fig. 5, including the artificial resonance peak around 0.8 GHz. It demonstrates the large resonance peak (shown by Eq. (1)) in the transverse impedance.

On the other hand, a disadvantage of the scheme using the shifted single wire is to produce the artificial resonances in the results. Consequently, a special care should be taken to compare the measurement result with the theoretical transverse impedance.

As shown in the left figure of Fig. 6, the ceramic break of MR is routinely covered by 12 capacitors. The impedance of one capacitor is measured, and it behaves like an inductor (~ 34.5 nH) at high frequency. The transverse impedance is simulation by CST, by assuming that 12 inductors cover the ceramic break. The result is shown in the right figure of Fig. 6. The 16 kΩ/m peak at 0.4 GHz in Fig. 2 is reduced to the 4.5 kΩ/m peak at 0.7 GHz in Fig. 6 at MR.

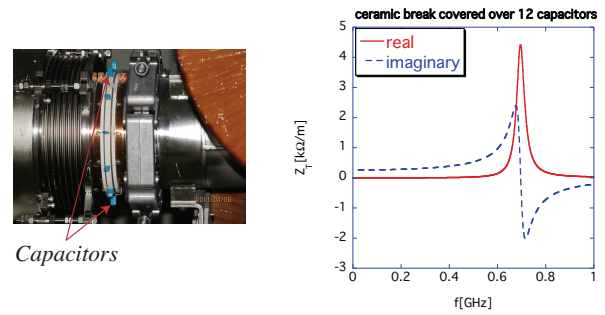


Figure 6: The ceramic break covered over 12 capacitors (left) and the simulation results of the transverse impedance by CST Studio (right).

### IMPEDANCES OF A CERAMIC BREAK COATED WITH TiN

Finally, we theoretically analyze the impedances of a ceramic break, where the inner surface of the ceramic is coated with resistive material (TiN) with the conductivity  $\sigma_{TiN} (= 5.88 \times 10^6 S/m)$  and the thickness  $t$ . Numerical simulations are not suitable for the calculation of this kind of impedance, because extremely small mesh sizes are necessary (smaller than the thin TiN coating). In reality, typical coating size of TiN is a few ten nm in the ceramic break.

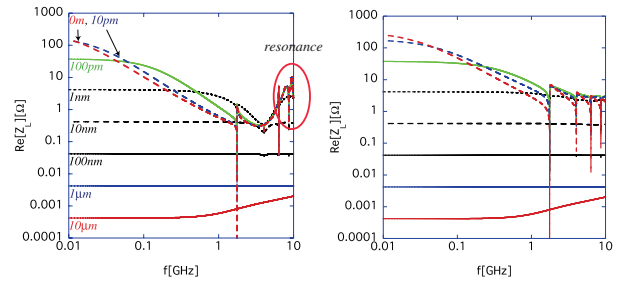


Figure 7: The thickness dependence of the longitudinal impedances of the ceramic break ( $\epsilon' = 11$ ) with the TiN coating (left) and that of the resistive insert without the ceramic ( $\epsilon' = 1$ , right) for the size of  $a = 65$  mm,  $a_2 = 70$  mm and  $g = 10$  mm.

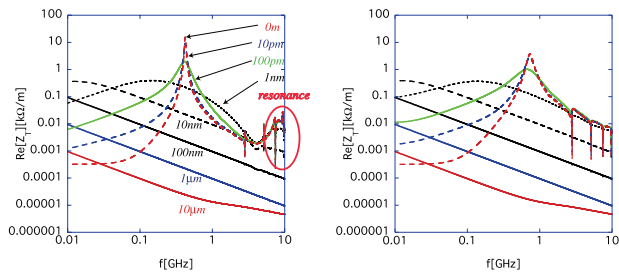


Figure 8: The thickness dependence of the transverse impedances of the ceramic break ( $\epsilon' = 11$ ) with the TiN coating (left) and that of the resistive insert without the ceramic ( $\epsilon' = 1$ , right) for the size of  $a = 65$  mm,  $a_2 = 70$  mm and  $g = 10$  mm.

Here, let us investigate the characteristic of the impedance with the thin TiN coating. Figures 7 and 8 show the longitudinal and the transverse impedances, respectively. The thickness dependence of the impedances is shown both for the ceramic break ( $\epsilon' = 11$ ) with the TiN coating and the corresponding thin resistive insert without the ceramic ( $\epsilon' = 1$ ) for the same size of gap. With the help of the discussion of the previous study [15], let us categorize the impedances of the ceramic break with the TiN coating for various TiN thickness. The frequency parameter  $f_\delta$  (the frequency at which the skin depth is equal to the TiN thickness) is introduced as

$$f_\delta \equiv \frac{c}{\pi Z_0 \sigma_c t^2}, \quad (8)$$

and the thickness parameter  $t_{min}$  is as

$$t_{min} \equiv \left( \frac{4g}{\pi^2 Z_0^3 \sigma_c^3} \right)^{\frac{1}{4}}, \quad (9)$$

which is typically of the order of a few ten nm in the short ceramic break.

In all the cases, the TiN coating is sufficiently thin so that its thickness is less than the skin depth within the frequency frame of the figures ( $f < 10$  GHz) except the  $t = 10 \mu\text{m}$  case where the skin depth starts to fall short of the TiN thickness above  $f_\delta$  ( $\sim 1$  GHz). When the TiN coating is thick enough ( $t > t_{min}$ ), but less than the skin depth, the entire image current runs on the TiN coating, and the impedance becomes proportional to  $1/t$ . Since the TiN coating almost perfectly shields the electromagnetic fields inside the beam chamber from leaking out to the ceramic, the appearance of resonances inside the ceramic is greatly suppressed. When the TiN coating is much thinner than  $t_{min}$  (e.g.  $t < 1$  nm), the electromagnetic fields starts to leak out through the TiN coating, and the existence of the ceramic and their resonance structures start to form the impedance (the left figures in Figs. 7 and 8).

## SUMMARY

The theoretical and numerical simulation results calculated by ABCI and CST Studio are compared. They are all in good agreement for the ceramic break without the TiN coating. Particularly, the agreements between the theoretical and ABCI's results are excellent, while CST Studio tends to provide higher impedances, notably at resonance frequencies, than the others.

The impedance of the ceramic break has resonance structures, because the difference of the dielectric constants between ceramic and the vacuum introduces the reflection

of waves at their boundaries, and this reflection of electromagnetic fields at the lower and the upper boundaries of the ceramic creates trapped modes inside. The resonances can be categorized into the cavity-mode resonances and the coaxial-mode resonances.

Bench measurements have been done for the evaluation of the transverse impedance of the ceramic break. The measurement results demonstrate the existence of the large resonance peak at low frequency (0.4 GHz).

The theory can be applied to the calculation of the impedance of a ceramic break whose inner surface is coated with thin TiN. When the TiN coating is thick (larger than  $t_{min}$ ), the entire image current runs in the TiN coating, which shields wake fields inside the chamber from reaching out to the ceramic. In this case, the existence of ceramic has no effect on the impedance. Consequently, the impedance becomes higher as the TiN becomes thinner.

## REFERENCES

- [1] Y. Shobuda *et al.*, Physical Review ST Accelerators and Beams, **12**, 032401, (2009).
- [2] K. Ohmi *et al.*, Physical Review ST Accelerators and Beams, **5**, 114402, (2002); PRST, **6**, 029901(E), (2003).
- [3] Y.H. Chin *et al.*, in *proceedings of HB2006*, 125, Tsukuba, Japan, (2006).
- [4] A.W. Chao, *Physics of collective beam instabilities in high energy accelerators*, Wiley, New York, (1993).
- [5] *Handbook of Accelerator Physics and Engineering* edited by A.W. Chao and M. Tigner, World Scientific, Singapore, (1999).
- [6] <http://j-parc.jp/index-e.html>
- [7] Y. Shobuda *et al.*, Physical Review ST Accelerators and Beams, **17**, 091001, (2014).
- [8] Y. Shobuda *et al.*, Physical Review ST Accelerators and Beams, **10**, 044403, (2007).
- [9] Y. H. Chin, KEK Report 2005-06, (2005).
- [10] CST STUDIO SUITE, <https://www.cst.com/>
- [11] M. Abramowitz and I. Stegun, *Handbook of mathematical functions—with formulas, graphs, and mathematical tables*, (Dover Pub., New York, 1974).
- [12] N. Biancacci *et al.*, Physical Review ST Accelerators and Beams, **17**, 021001, (2014).
- [13] G. Nassibian and F. Sacherer, NIMA **159**, 21, (1971).
- [14] <http://www.agilent.com/home>
- [15] Y. Shobuda *et al.*, Physical Review ST Accelerators and Beams, **12**, 094401, (2009).